J. Fluid Mech. (2005), *vol.* 536, *pp.* 1–25.
doi:10.1017/S0022112005004738 Printed in the United Kingdom

Wall-induced forces on a rigid sphere at finite Reynolds number

By LANYING ZENG[1], S. BALACHANDAR[1] AND PAUL FISCHER[2]

[1]Department of Theoretical and Applied Mechanics, University of Illinois at Urbana-Champaign, IL 61801, USA

[2]Mathematics and Computer Science Division, Argonne National Laboratory, Argonne, IL 60439, USA

(Received 5 May 2004 and in revised form 1 October 2005)

We perform direct numerical simulations of a rigid sphere translating parallel to a flat wall in an otherwise quiescent ambient fluid. A spectral element method is employed to perform the simulations with high accuracy. For $Re < 100$, we observe the lift coefficient to decrease with both Reynolds number and distance from the wall. In this regime the present results are in good agreement with the low-Reynolds-number theory of Vasseur & Cox (1977), with the recent experiments of Takemura & Magnaudet (2003) and with the simulations of Kim *et al.* (1993). The most surprising result from the present simulations is that the wall-induced lift coefficient increases dramatically with increasing Re above about 100. Detailed analysis of the flow field around the sphere suggests that this increase is due to an imperfect bifurcation resulting in the formation of a double-threaded wake vortical structure. In addition to a non-rotating sphere, we also simulate a freely rotating sphere in order to assess the importance of free rotation on the translational motion of the sphere. We observe the effect of sphere rotation on lift and drag forces to be small. We also explore the effect of the wall on the onset of unsteadiness.

1. Introduction

Particles are often subjected to a hydrodynamic lift force, and as a result they acquire a component of velocity transverse to the flow streamlines. The transverse motion, although much weaker than the streamwise particle motion, plays an important role in processes such as deposition and resuspension.

There are several sources of hydrodynamic lift force. A particle in shear flow experiences shear-induced lift force (Saffman 1965). From the properties of creeping flow it is well known that there is no lift force in a shear flow in the zero Reynolds number limit. The shear-induced lift force is clearly an inertial effect.

A spinning particle experiences a Magnus lift force when subjected to a uniform cross-flow (Rubinov & Keller 1961). This rotation-induced lift force can also be explained as an inertial effect arising from the differential pressure associated with the high-speed and low-speed sides of the sphere.

A particle moving parallel to a flat wall experiences a wall-normal lift force at non-zero finite Reynolds numbers. The wall-induced lift force is due to two competing mechanisms (Takemura & Magnaudet 2003). First, the vorticity generated at the surface of the particle advects and diffuses downstream. The presence of a

nearby wall breaks the axisymmetry of the wake vorticity distribution. The resulting induced velocity also breaks the symmetry and results in an effective lift force that tends to move the particle away from the wall. Second, from inviscid theory one can argue that the flow relative to the particle will accelerate faster in the gap between the particle and the wall. The resulting low pressure in the gap will induce a lift force directed toward the wall. Analytical expressions for the combined wall-induced lift force at low, but finite, Reynolds numbers have been obtained by Cox & Hsu (1977) and Vasseur & Cox (1977) for a rigid spherical particle with a no-slip surface and by Takemura *et al.* (2002) for a clean bubble with a stress-free surface.

Here we focus on the wall-induced lift force in the finite Reynolds number regime. For the general case of a particle in arbitrary translational and rotational motion through a boundary layer adjacent to a wall, all three lift mechanisms are simultaneously operative. We isolate the wall-induced lift mechanism by considering the steady translational motion of a rigid sphere parallel to a wall in an otherwise stagnant fluid. A physical scenario for such steady parallel motion is when a spherical particle gravitationally settles parallel to a flat plate that is slightly tilted away from the vertical. In this case, the hydrodynamic drag and lift forces on the sphere are in perfect balance with the components of the gravitational force. When particle motion is either unsteady or not parallel to the wall, the present results approximately apply only for the quasi-steady component of the force, which depends on the instantaneous position and velocity of the particle. In many situations, this quasi-steady component may itself provide an adequate measure of the actual force. In cases where the quasi-steady component is not adequate, one faces the difficult task of characterizing the effect of unsteady and non-parallel motion.

In this paper we present results from direct numerical simulations of a spherical particle in translational motion parallel to a rigid flat wall. The simulations are performed using a high-order spectral element method. The recent experiments of Takemura & Magnaudet (2003) are of great relevance to the present work, because they provide the first (and, to our knowledge, the only) clean measurement of wall-induced lift force over a wide range of Re. For Reynolds numbers of order unity, the experimental results are in excellent agreement with the low-Reynolds-number theory. On increasing Reynolds number up to about 100, Takemura & Magnaudet (2003) observe the lift coefficient to steadily decrease, but due to the finite Reynolds number effect, the decrease is milder than that predicted by the low-Reynolds-number theory. The present computational results, for $Re < 100$, are in good agreement with the experimental results of Takemura & Magnaudet. With further increase in Reynolds number the computations show an interesting trend of turnaround, and the lift coefficient begins to increase with Re. The increase is substantial enough to strongly influence the wall-normal motion of particles.

The wall-induced asymmetry of the flow, which is responsible for the lift force, also induces rotational motion as the particle translates parallel to the wall. In an unbounded linear shear flow, in the limit of low Reynolds number, Saffman (1965) has shown that the rotation-induced lift force is less important than the shear-induced lift force. At finite Re, recent numerical simulations (Bagchi & Balachandar 2002) have shown that the effect of free rotation on the translational motion of a particle is quite small. Furthermore, they have shown that the small added lift force due to rotation can be expressed as a scaled Magnus lift force. Here we similarly examine the importance of particle rotation in the presence of wall effect. In addition to a non-rotating sphere we consider a sphere that is free to rotate in response to the net

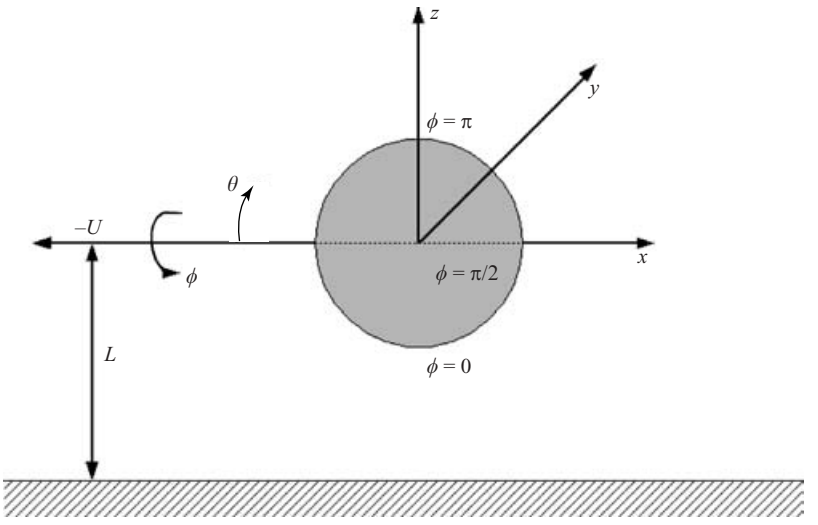

FIGURE 1. Schematic of a sphere moving through a stationary ambient fluid parallel to a flat wall. The coordinate system to be employed is shown.

hydrodynamic torque acting on it, in order to address the combined effect of rotation and wall-induced lift force.

In the unbounded case, the wake behind the sphere remains axisymmetric up to a Reynolds number of about 212. Above this the wake becomes non-axisymmetric, but there still exists a plane of symmetry whose orientation is arbitrary. The wake becomes unsteady and begins to shed vortices only above a Reynolds number of about 270 (Natarajan & Acrivos 1993; Johnson & Patel 1999; Bagchi, Ha & Balachandar 2001). With the presence of a nearby wall, the axisymmetry of the wake is geometrically broken at all Reynolds numbers. However, at low Reynolds numbers there exists a plane of symmetry that is normal to the wall, oriented along the streamwise direction, and passing through the centre of the particle. The present study will also include simulations of flow over a particle near a plane wall in the unsteady regime to examine the effect of the wall on the onset of unsteadiness.

2. Methodology

We consider a rigid sphere moving at a constant velocity $-U$ parallel to a flat wall in an otherwise quiescent ambient fluid, as shown in figure 1. We consider a reference frame attached to the particle. In this moving frame, the flat wall and the far field translate at a uniform velocity of U. We choose the diameter of the sphere, d, as the length scale and U as the velocity scale.

The governing equations in non-dimensional terms are

$$\nabla \cdot \boldsymbol{u} = 0, \tag{1}$$

$$\frac{\partial \boldsymbol{u}}{\partial t} + \boldsymbol{u} \cdot \nabla \boldsymbol{u} = -\nabla p + \frac{1}{Re} \nabla^2 \boldsymbol{u}. \tag{2}$$

The appropriate boundary conditions in the translating reference frame attached to the centre of the sphere are

$$\boldsymbol{u} = \boldsymbol{r} \times \boldsymbol{\Omega} \quad \text{for} \quad |\boldsymbol{r}| = 1/2, \tag{3}$$

$$\boldsymbol{u} = \boldsymbol{e}_x \quad \text{for} \quad z = -L, \tag{4}$$

$$\boldsymbol{u} = \boldsymbol{e}_x \quad \text{as} \quad |\boldsymbol{r}| \to \infty, \tag{5}$$

where $\boldsymbol{r}$ is the position vector from the centre of the sphere and $\boldsymbol{\Omega}$ is the non-dimensional angular velocity of the sphere. If the sphere is not allowed to rotate, then $\Omega = 0$. The two non-dimensional parameters of the problem are the Reynolds number, $Re = dU/\nu$, and the scaled distance from the wall, L, where ν is the kinematic viscosity of the fluid. In the present work, Re ranges from 0.5 to 300, and the values of L considered are 0.75, 1, 2, and 4.

The drag, lift, and moment coefficients are defined as follows:

$$C_D = \frac{\tilde{F}_D}{\left(\frac{1}{2}\rho U^2 \pi R^2\right)} = \frac{8}{\pi}\left[\int_S (-p\boldsymbol{n} + \boldsymbol{n}\cdot\boldsymbol{\tau})\,\mathrm{d}s\right]\cdot\boldsymbol{e}_x, \tag{6}$$

$$C_L = \frac{\tilde{F}_L}{\left(\frac{1}{2}\rho U^2 \pi R^2\right)} = \frac{8}{\pi}\left[\int_S (-p\boldsymbol{n} + \boldsymbol{n}\cdot\boldsymbol{\tau})\,\mathrm{d}s\right]\cdot\boldsymbol{e}_z, \tag{7}$$

$$C_M = \frac{\tilde{\boldsymbol{M}}\cdot\boldsymbol{e}_y}{\left(\frac{1}{2}\rho U^2 \pi R^3\right)} = \frac{16}{\pi}\left[\int_S \boldsymbol{r}\times\boldsymbol{\tau}\,\mathrm{d}s\right]\cdot\boldsymbol{e}_y, \tag{8}$$

where S denotes the surface of the sphere, $\boldsymbol{n}$ is the outward unit normal to the surface of the sphere, and $\boldsymbol{\tau}$ is the dimensionless viscous stress tensor. In these equations $\tilde{F}_D$, $\tilde{F}_L$, and $\tilde{\boldsymbol{M}}$ are the dimensional streamwise force, wall-normal force, and hydrodynamic moment on the particle, respectively. At the Reynolds numbers under consideration, symmetry about the $y = 0$ plane is preserved by the flow. As a result, there is no net force on the sphere along the y-direction. Furthermore, only the y-component of the moment is non-zero and is defined to be positive in the counter-clockwise direction.

3. Numerical approach and validation

We performed direct numerical simulations using NEK5000, which employs a $P_N - P_{N-2}$ spectral element method, which is a higher-order weighted residual technique that employs compatible trial and test spaces for velocity and pressure (Fischer 1997). The computational domain is partitioned into hexahedral elements, which are deformed by isoparametric mappings. Within each element, velocity and pressure are represented in local Cartesian coordinates by tensor-product Lagrange polynomials of degree N and $N-2$, respectively. Time stepping is based on a semi-implicit splitting scheme that, with correct treatment of the incompressibility constraint, allows high-order temporal accuracy. Computational complexity is significantly reduced by dividing the time advancement into independent convective, viscous, and pressure subproblems. The latter two subproblems are elliptic, which are solved efficiently by using the overlapping Schwarz method (Fischer 1997).

The computational domain is chosen to be a large rectangular box surrounding the sphere. Along the wall-normal direction the computational domain extends from the wall ($z = -L$) to a top boundary placed at $z = L_z$. Along the streamwise direction the computational domain extends from $x = -L_{xu}$ upstream of the sphere to $x = L_{xd}$ downstream of the sphere. Along the spanwise direction the computational domain extends on only one side of the sphere from $-7 \leqslant y \leqslant 0$, and a symmetry condition is enforced about the midplane $y = 0$. The appropriateness of this symmetry condition is verified with corresponding simulations performed over the entire span from $y = -7$ to $y = 7$. Disturbances that are asymmetric about the midplane were introduced, but

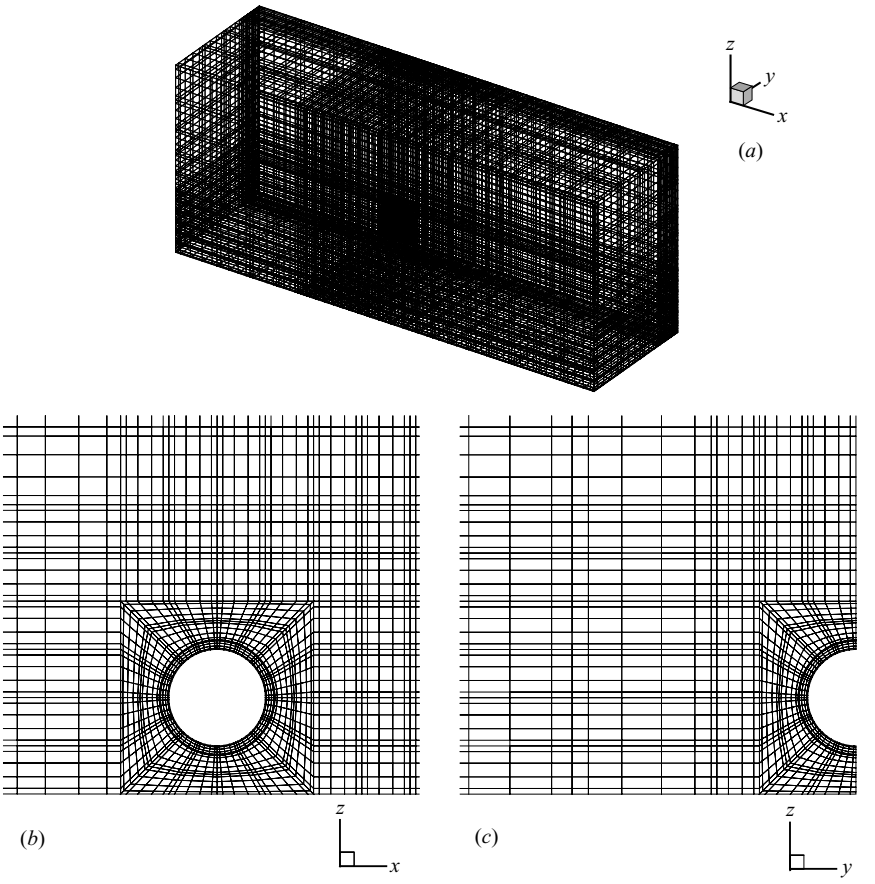

FIGURE 2. Sample spectral element discretization of the computational domain for the $L = 1$ case. (a) The entire computational domain; (b) zoom of the discretization near the sphere on the (x, z)-plane; (c) zoom of the discretization near the sphere on the (y, z)-plane.

the disturbances decayed, even for the unsteady cases at the highest Reynolds number of 300 considered here. Thus, symmetry about the midplane is maintained for all cases to be discussed. At the upstream end of the computational domain ($x = -L_{xu}$), the inflow condition, $\boldsymbol{u} = U\boldsymbol{e}_x$, is applied. At the downstream end a convective outflow boundary condition is applied. At the top and lateral boundaries we enforce $\partial \boldsymbol{u}/\partial z = 0$ and $\partial \boldsymbol{u}/\partial y = 0$, respectively. On the bottom plate a no-slip, no-penetration boundary condition in the moving frame of reference, $\boldsymbol{u} = U\boldsymbol{e}_x$, is applied.

The results presented here are obtained with a large computational domain given by $L_z = 8$, $L_{xu} = 8$, $L_{xd} = 16$ (this domain will be referred to as D1). A total of 1696 spectral elements are used to discretize the computational domain (see figure 2), and within each element a polynomial expansion of $5 \times 5 \times 5$ is used. The placement of top, upstream, and downstream boundaries of the computational domain is likely to have the largest influence on the resulting flow and the hydrodynamic force and torque on the sphere. To verify the adequacy of the above domain, we also performed simulations in a larger domain (D2) given by $L_z = 12$, $L_{xu} = 8$, $L_{xd} = 24$. The larger domain was discretized with 2296 spectral elements of $5 \times 5 \times 5$ resolution. The cross-sectional area of the sphere as seen by the flow is only 0.65 % of the cross-sectional area of the computational domain D1 and only 0.44 % for the larger domain D2.

		Smaller domain (D1)	Larger domain (D2)
$Re = 10$	C_D	4.721	4.717
	C_L	3.511×10^{-1}	3.510×10^{-1}
	C_M	1.512×10^{-2}	1.480×10^{-2}
$Re = 200$	C_D	8.156×10^{-1}	8.152×10^{-1}
	C_L	6.003×10^{-2}	6.000×10^{-2}
	C_M	1.346×10^{-3}	1.300×10^{-3}

TABLE 1. Effect of the size of the computational domain on the drag, lift, and moment coefficients for $L = 1$.

		$5 \times 5 \times 5$	$9 \times 9 \times 9$
$Re = 10$	C_D	4.721	4.721
	C_L	3.511×10^{-1}	3.512×10^{-1}
	C_M	1.512×10^{-2}	1.513×10^{-2}
$Re = 200$	C_D	8.156×10^{-1}	8.172×10^{-1}
	C_L	6.003×10^{-2}	6.070×10^{-2}
	C_M	1.346×10^{-3}	1.342×10^{-3}

TABLE 2. Effect of resolution, varied in terms of the order of polynomial expansions within each spectral element, on the drag, lift, and moment coefficients.

Thus the blockage effect is likely to be minimal for both the computational domains. Care was taken to maintain the level of resolution the same in both domains D1 and D2. Drag, lift, and moment coefficients, for $Re = 10$ and 200, computed with the two different domains for the case of a particle centred one diameter away from the plate ($L = 1$), are reported in table 1. From table 1, it is clear that the domain D1 is sufficient for accurately evaluating the drag, lift, and moment coefficients. Furthermore, the size of the computational domain is well within the acceptable range established in earlier studies of unbounded ambient flow over a sphere (Kim, Elghobashi & Sirignano 1993; Johnson & Patel 1999; Bagchi *et al.* 2001).

We address the adequacy of resolution by comparing the results obtained from two different orders of polynomial expansion. Table 2 lists drag, lift, and moment coefficients for $Re = 10$ and 200 at $L = 1$ for polynomial expansions of order $5 \times 5 \times 5$ and $9 \times 9 \times 9$. Comparing the two columns, one can observe that the maximum difference is 0.20 % for drag coefficient, 1.1 % for lift coefficient, and 0.30 % for moment coefficient. Therefore, the resolution of $5 \times 5 \times 5$ is employed in this study.

4. Results and discussion

4.1. *Flow field*

Figure 3 shows the streamlines around the sphere on the $y = 0$ symmetry plane for $Re = 2, 10$ and 200 at $L = 0.75$ and for $Re = 200$ at $L = 2$. On the symmetry plane the spanwise component of velocity, w, is zero and therefore fluid elements on this plane never leave the plane. The presence of the wall breaks the axisymmetry of the flow around the sphere, which is evident at all Re for the $L = 0.75$ case. As the distance from the wall increases, at $L = 2$, asymmetry in the streamlines is subtle but can be observed. At the lower Reynolds numbers the flow around the sphere remains attached, and for $Re = 200$ a recirculation region can be seen in the wake; but unlike

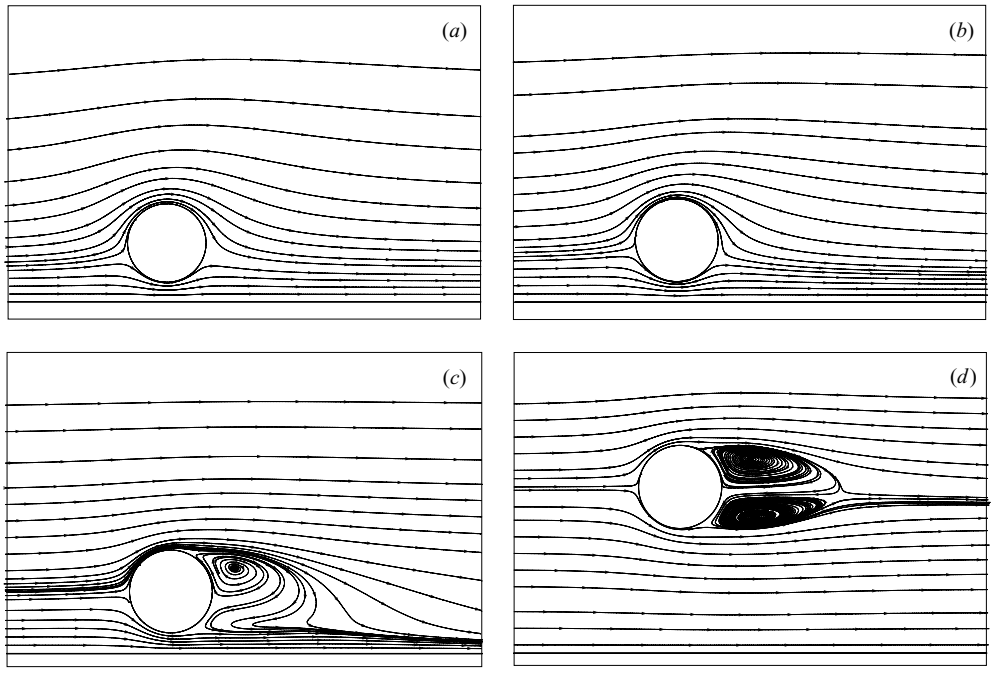

FIGURE 3. Streamlines plotted along the symmetry plane $y=0$: (*a*) $Re=2$, $L=0.75$; (*b*) $Re=10$, $L=0.75$; (*c*) $Re=200$, $L=0.75$; (*d*) $Re=200$, $L=2$.

in a uniform flow, significants asymmetry can be observed in the wake structure at $L=0.75$. In particular, due to asymmetry, the flow continues to accelerate even downstream of the gap between the wall and the particle. This effect is not as strong at $L=2$.

Figure 4 shows the distribution of the pressure coefficient, defined as $C_p=(p-p_\infty)/(\frac{1}{2}\rho U^2)$, plotted around the sphere along the $y=0$ midplane for $Re=2$, 10, 100, and 200 at $L=1$. Here, a zero angle corresponds to the front of the sphere and an angle of 180° corresponds to the leeward side of the sphere; both the top and bottom surfaces of the sphere are plotted separately for comparison.

Without the wall, the pressure distribution is axisymmetric, and there is no difference between the top and bottom surfaces. For a fixed distance from the wall, the asymmetric effect of the wall decreases with increasing Reynolds number for Re up to 100. With further increase to $Re=200$, the pressure on the lower side is greater than that on the upper side for all θ. The effect of this subtle change on the lift force is discussed in § 4.3.

For the rigid sphere considered here, the surface distribution of shear stress is directly related to the tangential (θ) and azimuthal (ϕ) distributions of surface vorticity (see figure 1 for the definition of tangential and azimuthal coordinates). Figure 5 shows the surface distribution of ω_ϕ for $Re=2$, 10, 100, and 200 at $L=1$. The figure shows ω_ϕ along three lines where the $y=0$ and $z=0$ planes intersect the sphere. The solid line corresponds to the top of the sphere ($\phi=\pi$), the dashed line is along the bottom of the sphere ($\phi=0$), and the dash-dotted line is along the line where the $z=0$ plane intersects the sphere ($\phi=\pi/2$). The positive value of ϕ-vorticity over most of the sphere surface is due to the predominantly left to right ambient flow within the boundary layer over the sphere. This component of surface vorticity (and the

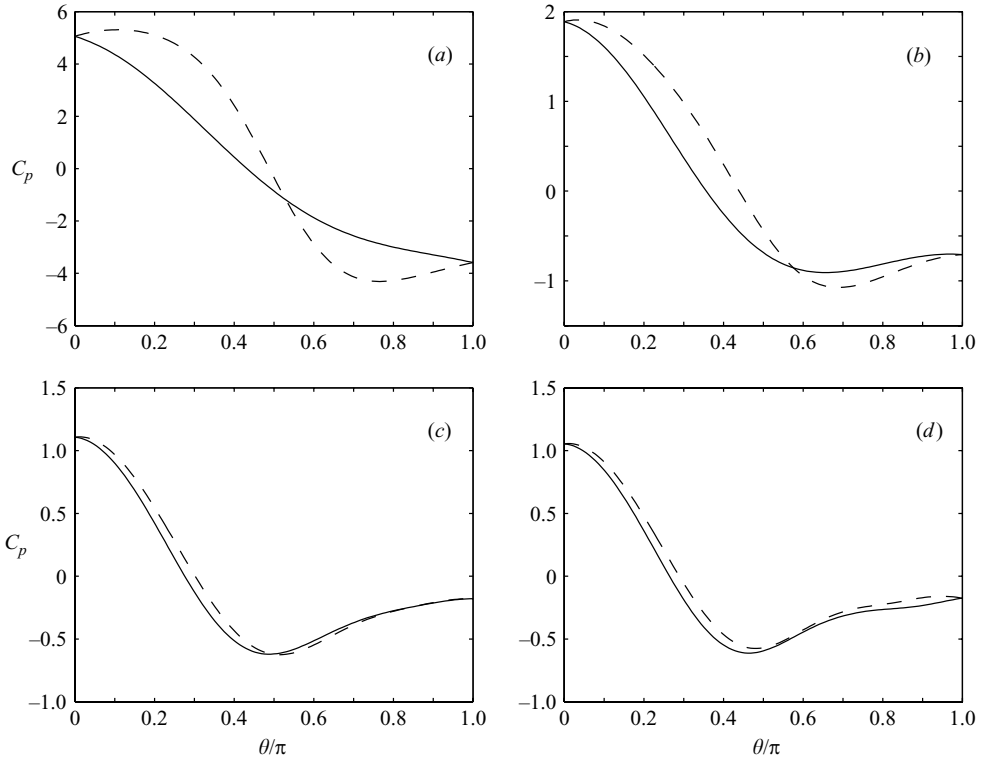

FIGURE 4. Distribution of the pressure coefficient around the sphere in the $y=0$ plane for $L=1$: (*a*) $Re=2$; (*b*) $Re=10$; (*c*) $Re=100$; (*d*) $Re=200$; ——, along the top of the sphere; - - -, along the bottom.

associated surface shear stress $\tau_{r\theta}$) entirely accounts for the skin friction component of the drag. In the absence of wall effect the surface distribution of ω_ϕ will be axisymmetric. The top–bottom asymmetry observed in figure 5 can contribute to a net z-force on the sphere.

At the lowest Reynolds number considered, the vorticity distribution is nearly symmetric about $\theta=\pi/2$, indicating fore–aft symmetry. As was observed in the streamlines in figure 3(*a*), the effect of the wall is to move down the front and rear stagnation points on the surface of the sphere below the poles toward the wall. This translates to a small positive (or negative) value for ω_ϕ on the upper (or bottom) side of the sphere as $\theta\to 0$ and π. The acceleration of the flow in the gap between the sphere and the plate results in a nearly 65 % increase in ω_ϕ at the bottom of the sphere compared to the top.

With increasing Reynolds number to $Re=10$, many of the features observed at the lower Reynolds number can still be observed, but departure from fore–aft symmetry is significant. Due to the thinning of the boundary layer, the magnitude of vorticity increases, and the peak azimuthal vorticity at the bottom of the sphere is only 15 % larger than its peak value at the top of the sphere. At $Re=100$ and 200 the negative surface azimuthal vorticity for $\theta>2\pi/3$ corresponds to flow separation and the presence of reversed flow along the surface of the sphere within the recirculating wake (see figure 3*c*). Unlike in the lower Reynolds number cases, at $Re=200$ the peak vorticity at the bottom of the sphere is slightly lower than its peak at the top.

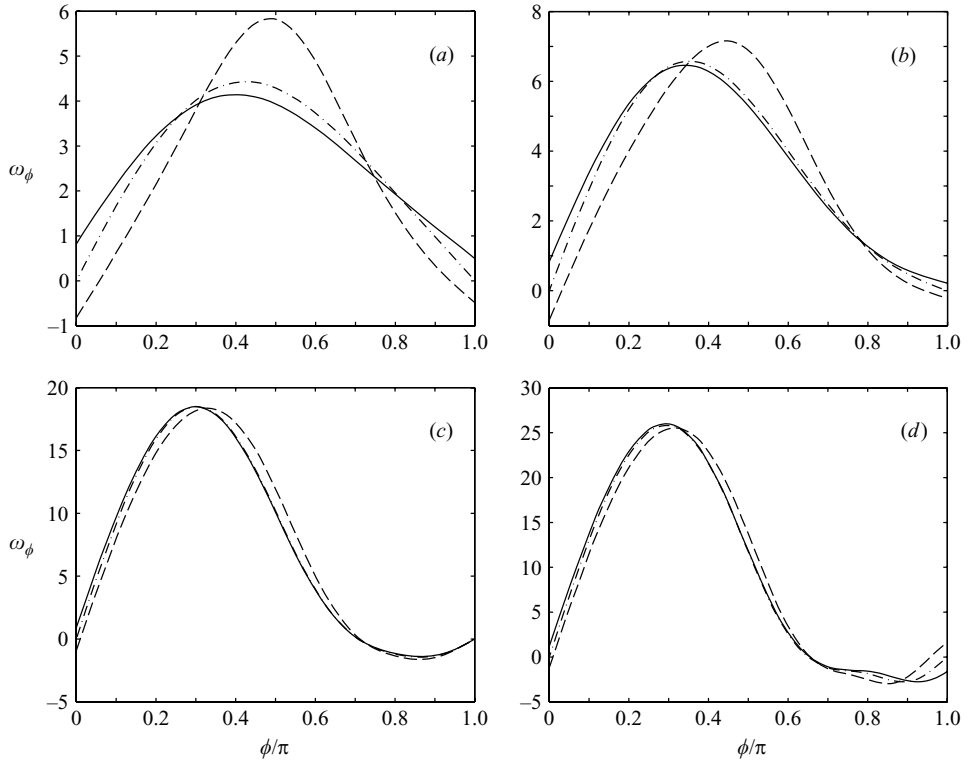

FIGURE 5. Distribution of ϕ-component of surface vorticity along the lines where the $z=0$ and $y=0$ planes intersect the sphere. All results are at $L=1$ for (*a*) $Re=2$; (*b*) $Re=10$; (*c*) $Re=100$; (*d*) $Re=200$; ——, top of the sphere where the $y=0$ plane intersects the sphere; - - -, along the bottom where the $y=0$ plane intersects the sphere; —·—, along the middle where the $z=0$ plane intersects the sphere.

Figure 6 shows the tangential component of surface vorticity along the line where the $z=0$ plane intersects the sphere. Owing to the symmetry of the flow about the $y=0$ plane, this component of vorticity is identically zero along the top and bottom of the sphere (i.e. along the two other lines shown in figure 5). Without the wall, the tangential component of vorticity, ω_θ, is identically zero, and thus the distribution of ω_θ is indicative of the degree of azimuthal flow induced by the symmetry-breaking effect of the wall. This component of vorticity and the associated azimuthal component of wall shear stress, $\tau_{r\phi}$, contribute only to the lift force.

On the $\phi=\pi/2$ plane, the sign (positive or negative) of ω_θ indicates the direction (down or up) of the z-component of the flow within the boundary layer around the sphere. Thus, at $Re=2$ the flow is directed slightly away from the wall on the windward side, but directed toward the wall on the leeward side. The direction of this flow is consistent with the downward shift in the front and rear stagnation points below the $z=0$ plane. At this low Reynolds number there is almost a fore–aft symmetry, and therefore there will be no net contribution to the lift force. With increasing Re the distribution of ω_θ is qualitatively the same on the windward side. However, due to the formation of the wake, the behaviour on the leeward side changes with Re. In particular, at $Re=100$, ω_θ remains negative along the entire $\phi=\pi/2$ line, thus indicating a positive z-component of the surface shear stress, which contributes

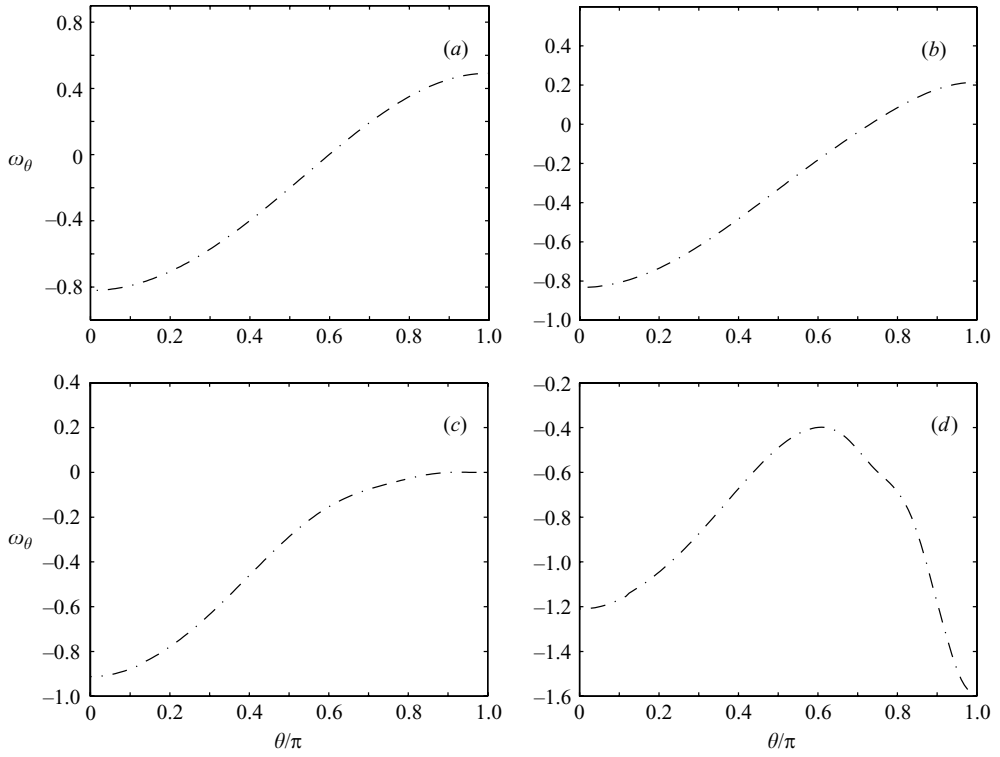

FIGURE 6. Distribution of the θ-component of surface vorticity along the line where the $z=0$ plane intersects the sphere. All results are at $L=1$ for (*a*) $Re=2$; (*b*) $Re=10$; (*c*) $Re=100$; (*d*) $Re=200$.

to a net lift force directed away from the wall. With further increase in Re above 100, a strong decrease in ω_θ is seen, and correspondingly a significant contribution to the positive z-force can be expected.

4.2. *Drag force*

Figure 7 shows the drag coefficient over the Reynolds number range 0.5 to 300 for varying separation distances between the particle and the wall. Also plotted for comparison in the figure as a solid line is the standard drag correlation (Schiller-Neumann formula; Clift, Grace & Weber 1978):

$$C_D = \frac{24}{Re}(1 + 0.15Re^{0.687}). \tag{9}$$

From figure 7, it is clear that for a sphere moving parallel to the wall the drag force on the sphere increases with decreasing distance between the sphere and the wall over the entire range of Reynolds number considered here. For $Re < 100$, the drag coefficient for all four separation distances considered here is larger than that given by standard drag. Thus, at this Reynolds number the effect of the wall is to increase the drag force. For $Re > 100$ we observe that when the sphere is very close to the wall (i.e. for $L=0.75$ and $L=1$) the effect of the wall still increases the drag coefficient. However, as the distance between the wall and the sphere increases (i.e. at $L=2$ and $L=4$), the drag coefficient is lower than that for an unbounded uniform flow, although only slightly.

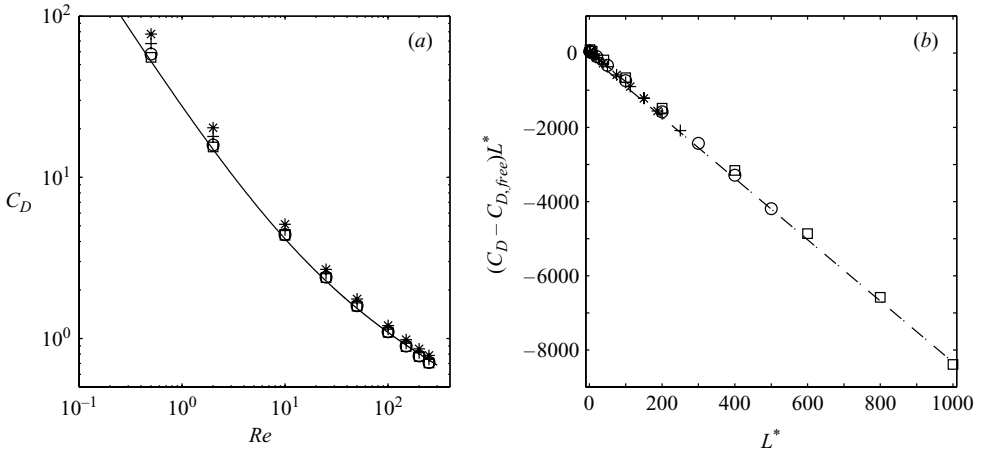

FIGURE 7. (*a*) Drag coefficient versus Re for the four different separation distances; (*b*) rescaled drag coefficient, $(C_D - C_{D,free})L^*$ against L^*; □, $L = 4$; ○, $L = 2$; +, $L = 1$; *, $L = 0.75$; ——, the standard drag correlation given in (9); — · —, curve fit $(C_D - C_{D,free})L^* = 66.654 - 8.364L^*$.

Kim *et al.* (1993) considered forces on a pair of spheres settling side by side in still fluid. They observed the drag coefficient to increase as the two spheres are very close to each other, but a close look at their results indicates that for intermediate separation distances the drag coefficient is slightly lower than its asymptotic value for a single isolated sphere. In the inviscid limit, the effect of a symmetry plane is to decrease the drag force (Kok 1993). It thus appears that for larger separations from the wall, the inviscid effect dominates the viscous effect to bring about a slight decrease in the drag force.

The increase in drag coefficient can be justified in terms of the added viscous effect arising from the presence of a nearby wall, but the slight decrease in drag coefficient with the presence of a wall can seem surprising. This trend was also observed in the low-Reynolds-number asymptotic results of Vasseur & Cox (1977) for a sphere sedimenting in a stagnant fluid bounded by a plane vertical wall. They observed that for small distances from the wall, measured in terms of $L^* = LRe \ll 1$, the drag coefficient increases, and for $Re \ll L^* \ll 1$ the asymptotic form of the increase can be expressed as

$$C_D - C_{D,free} = \frac{27}{4L^*}, \tag{10}$$

where $C_{D,free} = 24/Re(1 + (3/8)Re)$ is the asymptotic low-Reynolds-number drag coefficient in the absence of the wall. In contrast, as the distance from the wall increases, for $Re \ll 1 \ll L^*$ the asymptotic form of the decrease in drag coefficient was obtained as

$$C_D - C_{D,free} = -\frac{9\beta}{2(L^*)^{5/2}}, \tag{11}$$

where $\beta = 0.50698$. They explained this decrease in drag coefficient in terms of a potential flow induced by the inflow and outflow from the boundary layer on the wall, which close to the sphere is in the direction of its motion and thus reduces the effective settling velocity.

The present finite-*Re* results are only in qualitative agreement with the above low-*Re* asymptotic prediction. In figure 7(*b*) the computed finite-*Re* drag coefficient

is replotted as $(C_D - C_{D,free})L^*$ vs. L^*. The present numerical results can be well fitted by a straight line of the form $a+bL^*$, where the intercept $a = 66.654$ and the slope $b = -8.364$. The drag coefficient for the different distances from the wall and for varying Re collapses well in figure 7(b). The switch from above to below $C_{D,free}$ occurs at $L^* \approx 8$, which is consistent with the low-Re behaviour given by Vasseur & Cox (1977). For large values of L^* the drag coefficient reaches a constant value (0.736), and the approach to this constant value is as L^{*-1}, and not as $L^{*-5/2}$ as in the low-Re limit.

4.3. *Lift force*

Takemura & Magnaudet (2003) discussed two different mechanisms of lift force for the case of a sphere moving parallel to a wall in an otherwise stagnant fluid. The vorticity generated at the sphere surface advects and diffuses downstream and interacts with the wall, and this interaction results in a net lift force on the sphere directed away from the wall. On the other hand, the inviscid effect of the wall is to accelerate the fluid in the gap between the sphere and the wall and thus result in a local low pressure that corresponds to a net force on the sphere that is directed toward the wall. As observed by Takemura & Magnaudet, for a rigid sphere over the entire range of Reynolds number and distance from the wall, the first of the two mechanisms dominates, and as a result the net lift force on the sphere is directed away from the wall.

The lift force on the sphere as computed in the present simulations is presented below. Figure 8(a) shows the lift coefficient C_L vs. the scaled separation distance L^*. Also plotted in frame (a) as a thick solid line is the asymptotic result of Vasseur & Cox (1977):

$$C_L = \tfrac{9}{8}\left[1 - \tfrac{11}{32}L^{*2}\right]. \tag{12}$$

For small values of L^* (and correspondingly small values of Re) the computed C_L is in good agreement with the above asymptotic result. As observed in the experiments of Cherukat & McLaughlin (1990), (12) provides a good approximation even up to $L^* = 4$. With increasing L^* the lift coefficient decreases rapidly initially, but the rate of decrease at finite Reynolds number is consistently smaller than the asymptotic prediction of $(L^*)^{-2}$. In the limit of $Re \ll 1$ the lift coefficient depends only on L^*; however, as illustrated by the measurements of Takemura & Magnaudet (2003) at finite Re, the lift coefficient is a function of both L^* and Re (or L and Re). The increase in lift over the asymptotic prediction becomes large (for a fixed L^*) with decreasing distance from the wall or increasing Re.

Also shown in figure 8(a) are dotted lines that connect data points for fixed Re. As pointed out by Takemura & Magnaudet (2003), with increasing Reynolds number, from $Re \to 0$ to about $Re \approx 100$, the decay of the lift coefficient steadily increases from $C_L \propto (L^*)^{-2}$ to $C_L \propto (L^*)^{-3.4}$. This change in the decay rate has been elegantly argued by Takemura & Magnaudet (2003) as due to the change in the behaviour of the disturbance flow from that of a Stokeslet at low Re to that of a dipole at higher Re. However, with further increase in Reynolds number the decay rate decreases. This is clearly due to the fact that for a fixed separation distance from the wall, C_L does not continue to decrease with increasing L^*, but in fact begins to increase above a certain L^*. A careful look at the data shows that the turnaround occurs at Reynolds number between 100 to 150, at all the four separation distances considered. Despite this dramatic increase, at the highest Reynolds number considered ($Re = 250$), the lift coefficient is still an order of magnitude smaller than the $L^* \to 0$ limit of 9/8.

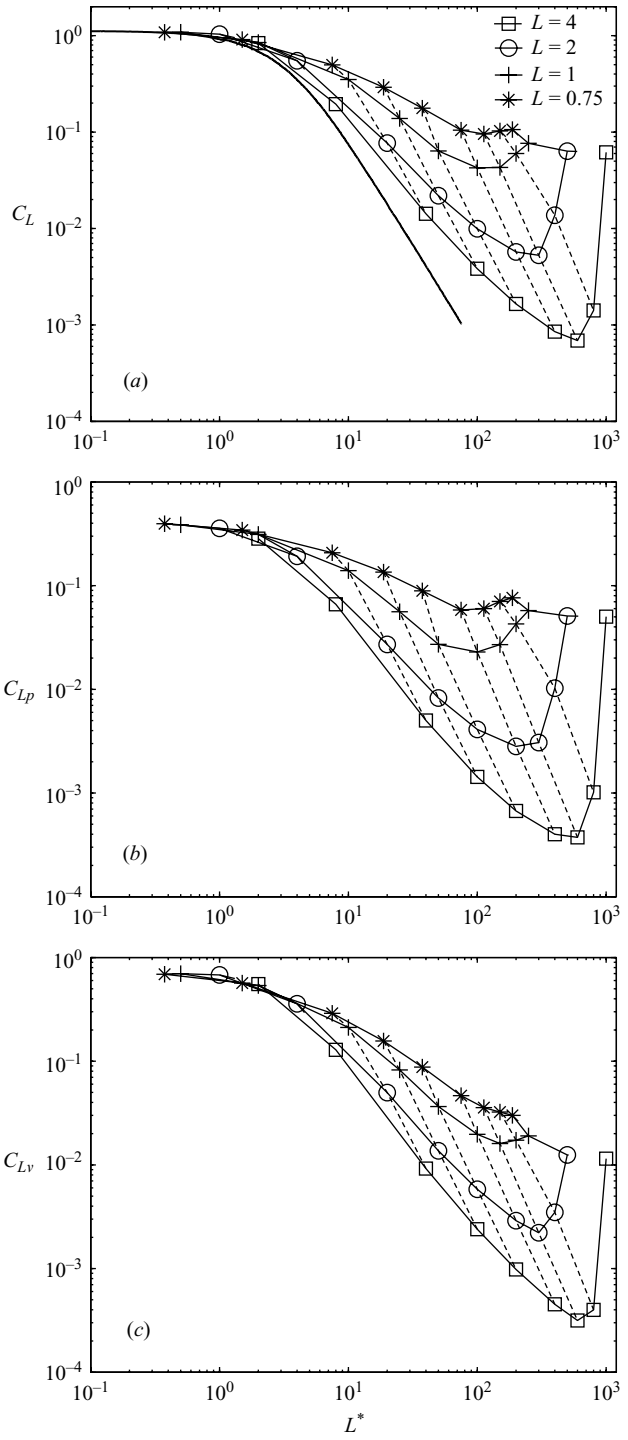

FIGURE 8. The wall-induced lift coefficient C_L vs. L^*: (*a*) overall lift coefficient C_L; (*b*) pressure-induced lift coefficient C_{Lp}; (*c*) viscous-induced lift coefficient C_{Lv}. The thick solid line is the analytical result from Vasseur & Cox (1977); symbols are the same as in figure 7; the dashed lines connect data for constant *Re*.

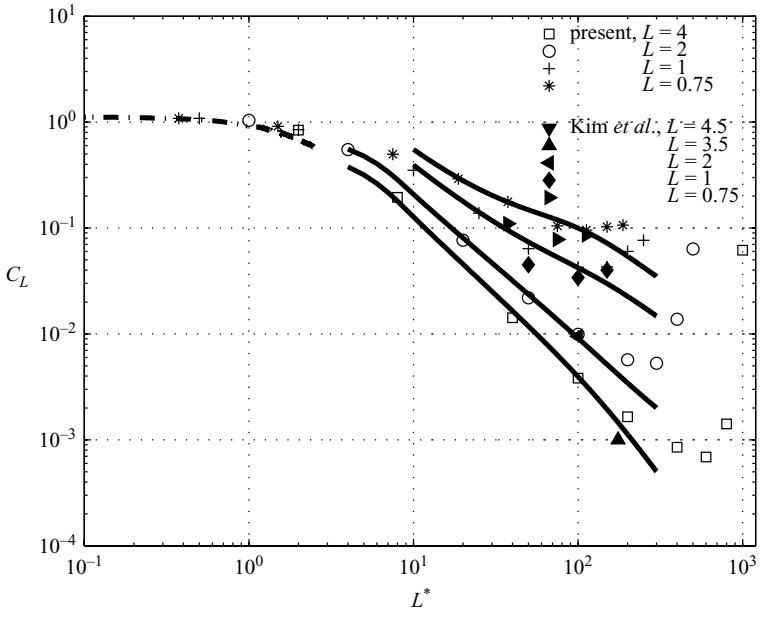

FIGURE 9. Lift coefficient C_L vs. L^*. Symbols for the present results are the same as in figure 7. $-\cdot-$, the low-Re asymptotic result of Vasseur & Cox (1977); ——, model (equations (13)–(15)) of Takemura & Magnaudet (2003) for $L = 0.75$, 1, 2 and 4. The solid symbols are data from Kim *et al.* (1993).

With further increase in Re the flow becomes unsteady, and the critical Reynolds number for onset of unsteadiness depends on the distance of the sphere from the wall. Simulations at higher Reynolds numbers in the unsteady regime indicate that the increase in C_L seen in figure 8(a) does not continue forever. Indications of this behaviour can be seen in the data for $L = 0.75$. Here we first limit attention to drag and lift forces in the steady regime.

In figure 8, frame (a) shows the total lift coefficient, while frames (b) and (c) show the pressure and skin friction contributions to the lift coefficient. As expected, at small values of L^* the dominant contribution is from skin friction, while at higher L^* (and correspondingly higher Re) the dominant contribution is from surface distribution of pressure. Both the pressure and skin friction contributions clearly show the initially decreasing and then increasing trend seen in the overall lift coefficient.

Takemura & Magnaudet (2003) summarized their experimental results with the following model for the lift coefficient:

$$C_L = C_{L0} a^2 (L/1.5)^{-2\tanh(0.01Re)}, \tag{13}$$

where

$$a = 1 + 0.6Re^{1/2} - 0.55Re^{0.08} \tag{14}$$

and

$$C_{L0} = \begin{cases} (9/8 + 5.78 \times 10^{-6} L^{*4.58})\beta^2 \exp(-0.292L^*) & \text{for} \quad 0 < L^* < 10 \\ 8.94\beta^2 L^{*-2.09} & \text{for} \quad 10 \leqslant L^* < 300. \end{cases} \tag{15}$$

Figure 9 compares this model with the lift coefficient obtained from the present simulations. The model is plotted only over the intended range of $L^* < 300$. For the

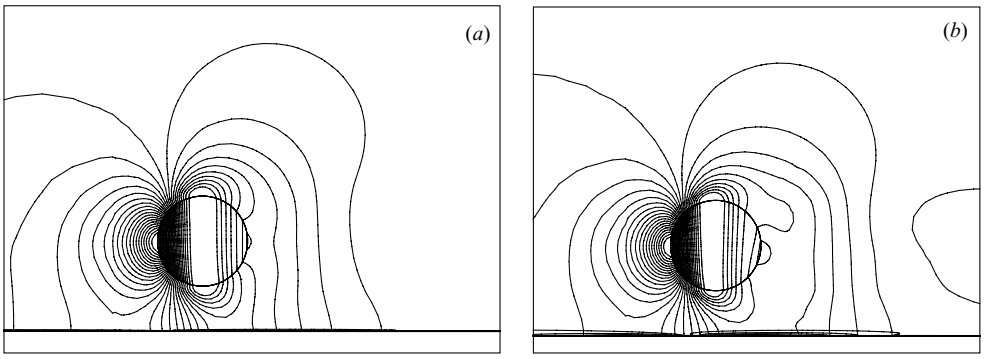

FIGURE 10. Contours of the pressure coefficient plotted on the $y = 0$ plane and on the surface of the sphere. (*a*) $Re = 100$; (*b*) $Re = 200$.

largest separation considered ($L = 4$), good agreement extends for about $L^* < 200$, and for the smallest separation ($L = 0.75$) good agreement can be observed for $L^* < 100$. For L^* much larger, the above model may underpredict lift coefficient by more than an order of magnitude. This result is not surprising since the experiments of Takemura & Magnaudet (2003) cover a range of Reynolds number from about 1 to 92, and in this range the agreement between the experimental and computational results is quite good.

The down-and-up evolution of C_L with increasing L^* is clearly surprising. The agreement with the results of Vasseur & Cox (1977) at small values of L^* and with the experiments of Takemura & Magnaudet (2003) at moderate L^* support the accuracy of the present simulations. Additional support comes from the simulations of Kim *et al.* (1993). For the case of two spheres settling side by side in a stagnant fluid, at a fixed Re, they observed the lift coefficient to be large and positive for small values of L. The lift coefficient decreased rapidly and took negative values as L increased above a threshold that depended on Re. Their results for $Re = 50$, 100, and 150 showed the down-and-up trend for separation distances $L = 0.75$ and 1. For larger separations the lift coefficient monotonically decreased from $Re = 50$ to 150. Their results are also plotted in figure 9 as solid symbols. Given the differences in configuration between the present simulations and those of Kim *et al.* (1993), the agreement is quite good.

The details of this down-and-up behaviour can be explored in terms of surface pressure and shear stress distributions shown in § 4.1. As seen in figure 4, with an increase in Re from 100 to 200, the pressure distribution on the leeward side changes significantly. The details of the pressure distribution (in terms of coefficient of pressure) on the $y = 0$ plane at these two Reynolds numbers are shown in figure 10. The change in pressure distribution on the leeward side is associated with the formation of a strong wake that is shifted and tilted down at $Re = 200$. This subtle change is responsible for the increase in the pressure component of the lift force.

The effect of the strong and somewhat tilted wake at $Re = 200$ can be seen in the surface vorticity distributions as well. In figure 5(*c*) for $Re = 100$ the surface vorticity was nearly zero at the rear of the sphere (angle = 180°). Whereas, for $Re = 200$, the non-zero azimuthal vorticity at this location indicates surface shear stress along the z-direction contributing positively to the lift force. The effect of this local flow directed away from the wall in the wake region can also be seen in figure 6 as the large negative tangential vorticity for angle $\rightarrow$ 180°. Thus, clearly the wake, through its

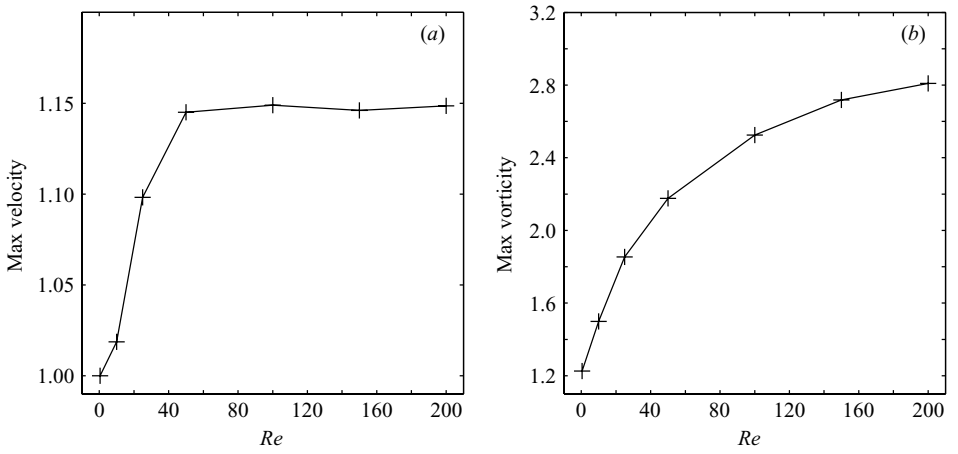

FIGURE 11. (*a*) Maximum velocity in the gap between the sphere and the wall and (*b*) maximum surface vorticity vs. Re for $L = 1$.

location and orientation, plays a significant role in increasing both the pressure and the skin friction contributions to lift.

The down-and-up trend in the lift coefficient can also be investigated in terms of the vorticity and inviscid mechanisms of lift. Figure 11 shows a plot of the maximum fluid velocity within the gap between the wall and the sphere as a function of Re for $L = 1$. We note that the maximum velocity also shows a change in trend around $Re = 100$. Below this Reynolds number the maximum velocity within the gap increases with Re. Correspondingly, the inviscid lift contribution, which is directed toward the wall, can be expected to increase. As Re increases above 100, the maximum velocity within the gap saturates, and the associated inviscid lift force can be expected to weaken. This behaviour of the maximum velocity is consistent with the down-and-up trend observed in the overall lift force, which is directed way from the wall.

Also plotted in figure 11 is the maximum surface vorticity obtained at $L = 1$ for the different Re cases. As expected, the surface vorticity generation increases steadily with Re. A closer look at the wake vortical structure is shown in figure 12, where the surface of constant swirling strength equal to 0.1 is plotted. Swirling strength is defined as the imaginary part of the complex eigenvalue of the velocity gradient tensor. As shown by Zhou *et al.* (1999) and Bagchi *et al.* (2001), it captures well the compact vortical structures. For each Reynolds number both the top view and side view of the three-dimensional vortex structure are shown. For $Re = 50$ a weak double thread can be seen in the wake. The double-threaded wake gains strength and extends farther downstream with increasing Reynolds number. Below a Reynolds number of 50 the double-threaded wake is absent.

In an unbounded uniform ambient flow, the flow remains axisymmetric at lower Reynolds numbers. At about $Re \approx 210$ there is a *perfect bifurcation* to a non-axisymmetric state in which the wake vortex structure takes the double-threaded shape (Natarajan & Acrivos 1993; Tomboulides 1993; Johnson & Patel 1999; Bagchi *et al.* 2001). The flow still remains steady, and a plane of symmetry passes through the centre of the sphere. The normal to this plane of symmetry must be orthogonal to the ambient flow direction, but its orientation is otherwise arbitrary and is dictated only by the initial condition. The double thread is one sided and results in a transverse (lift) force on the sphere.

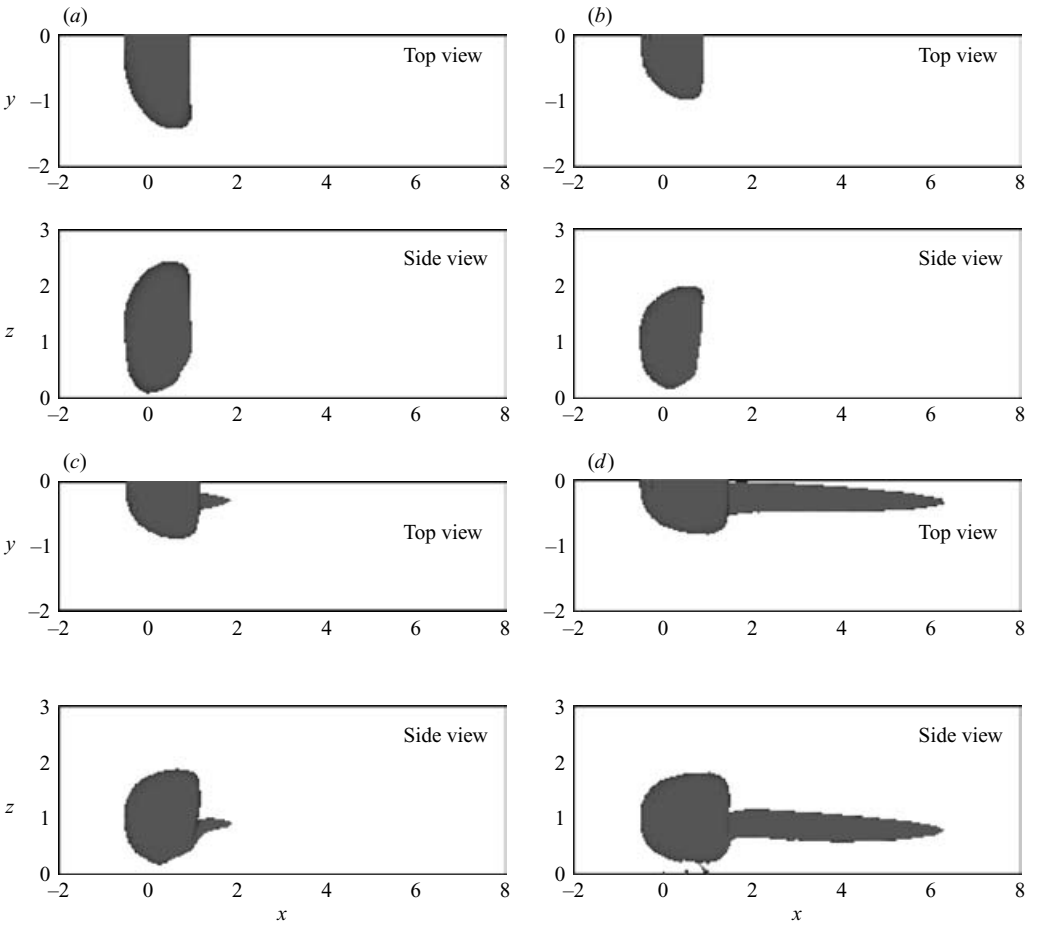

FIGURE 12. Wake vortical structure plotted as the surface of constant swirling strength equal to 0.1. Both the top and side views are shown. (*a*) $Re = 10$; (*b*) $Re = 50$; (*c*) $Re = 100$; (*d*) $Re = 200$.

With the presence of a nearby wall, the flow around the sphere is non-axisymmetric at all *Re*. However, from figure 12 we believe that the flow undergoes an *imperfect bifurcation* to a state involving double-threaded vortical structure in the wake region. At $L = 1$ this bifurcation appears to occur at *Re* below 50. Furthermore, the plane of symmetry is fixed to be wall normal (x, y-plane), and as a result the transverse force induced by the double-threaded wake vortex structure is in the z-direction. While the other wall-induced lift mechanisms are weakening with increasing *Re*, the double-threaded wake-induced lift force gains strength after the imperfect bifurcation. The increase in overall lift coefficient observed in figure 8(*a*) appears due to the double-threaded wake.

4.4. *Moment coefficient*

The symmetry-breaking effect of the wall induces a net hydrodynamic moment on the sphere about the y-axis. Figure 13 shows the moment coefficient versus Reynolds number for $Re > 10$. For smaller Reynolds numbers the moment coefficient, unlike the force coefficients, shows a much greater sensitivity and requires a much

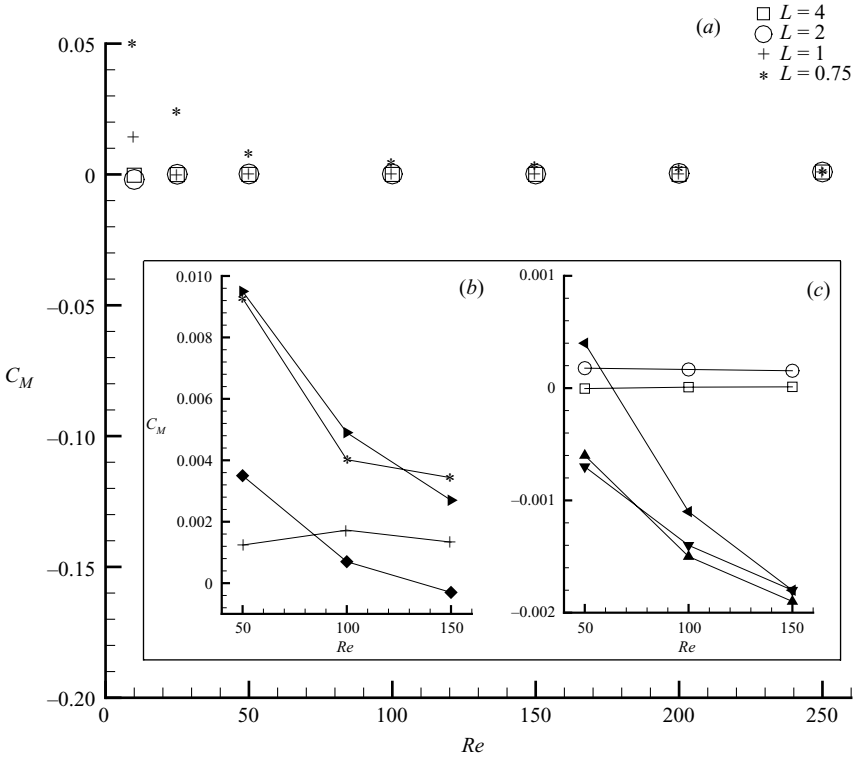

FIGURE 13. (*a*) Moment coefficient C_M vs. Re; (*b*), (*c*) results for large Re cases compared with those of Kim *et al.* (1993). Symbols are the same as in figure 9.

larger computational domain. The moment coefficient is in general small and rapidly decreases with both L and Re.

The inset in figure 13(*b*,*c*) shows the present moment coefficients at the higher Reynolds numbers compared with those obtained by Kim *et al.* (1993) for a pair of side-by-side spheres with a symmetry plane between them. Note that the present results for $L = 4$ are compared to their results for $L = 3.5$ and $L = 4.5$. The comparison is acceptable for the smallest separation considered. At larger separation distances, the two sets of results differ both qualitatively and quantitatively. Our moment coefficients are generally very small, remain positive, and are not strongly Reynolds-number dependent for $Re > 50$. In contrast, the results of Kim *et al.* (1993) continue to decrease with increasing Re and become negative at large Re. The accuracy of the present results has been adequately verified.

4.5. *Effect of free rotation*

A sphere in translational motion parallel to a flat wall tends to rotate about the y-axis passing through its centre. This rotation is in response to the hydrodynamic torque acting on the sphere, as outlined in the previous section. Depending on the sign of the torque, the rotation is either clockwise or counter-clockwise. In all the cases considered here so far, the sphere translated at a uniform velocity parallel to the wall but was not allowed to rotate. Now by allowing free rotation of the sphere, we investigate its effect on the flow field around it and the resulting forces. In the simulations discussed below, the starting condition is the corresponding 'no-rotation' case, and the sphere is subsequently allowed to angularly accelerate in response to

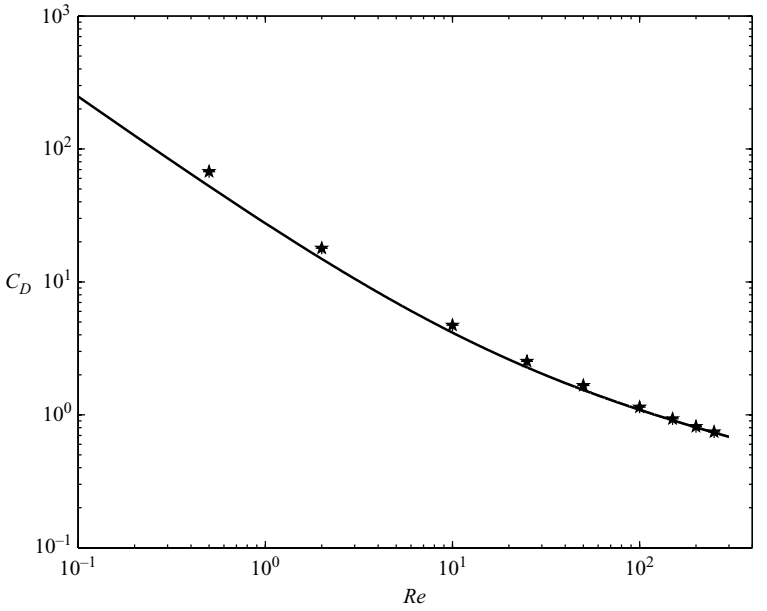

FIGURE 14. Drag coefficients for non-rotating and torque-free rotating spheres at $L = 1$: ——, standard drag (equation (9)); +, non-rotating; ★, torque-free rotating.

the hydrodynamic torque acting on it. In all the cases considered here, the sphere reaches a terminal angular velocity at which the hydrodynamic torque becomes zero. A comparison of this 'rotating' steady state with the 'non-rotating' steady state isolates the influence of torque-free rotation.

In response to the torque exerted on it, the free rotation of the sphere is in the clockwise direction, i.e. the sphere rotates such that, in the frame of reference moving with the particle, its rotation aids the ambient flow in the gap between the particle and the wall. This result at finite Re is in qualitative agreement with the low-Reynolds-number behaviour (Faxen 1921, 1924; Magnaudet, Takagi & Legendre 2003). Consistent with figure 13, the torque-free rotation rates are quite small. The computed drag coefficients for a non-rotating sphere and for the corresponding torque-free rotating sphere at $L = 1$ are plotted together with (9) in figure 14. The effect of free rotation is quite small over the entire range of L^*. The results for other separations are similar and therefore not shown here. This relatively minor influence of free rotation on the drag force is consistent with the asymptotic and low-Re experimental results of Cox & Hsu (1977) and Cherukat & McLaughlin (1994).

The little influence of sphere rotation on drag force is not surprising. Rotation is likely to have a stronger influence on the lift force. The computed lift coefficients for the torque-free rotating and non-rotating spheres at $L = 1$ are shown in figure 15. As $Re \to 0$, the percentile change in lift force due to torque-free rotation is quite small. In the context of an unbounded linear shear flow, for $Re \ll 1$, Saffman (1965) showed that rotation-induced lift force is asymptotically smaller than shear-induced lift force. The present results show a similar behaviour, i.e. for $Re \ll 1$ the rotation-induced lift force is asymptotically smaller than the wall-induced lift force. At larger Re the effect of torque-free rotation on lift, although still small, is measurable. Further separation of the total lift into pressure and skin friction contributions shows that the dominant effect of rotation comes from the surface distribution of pressure.

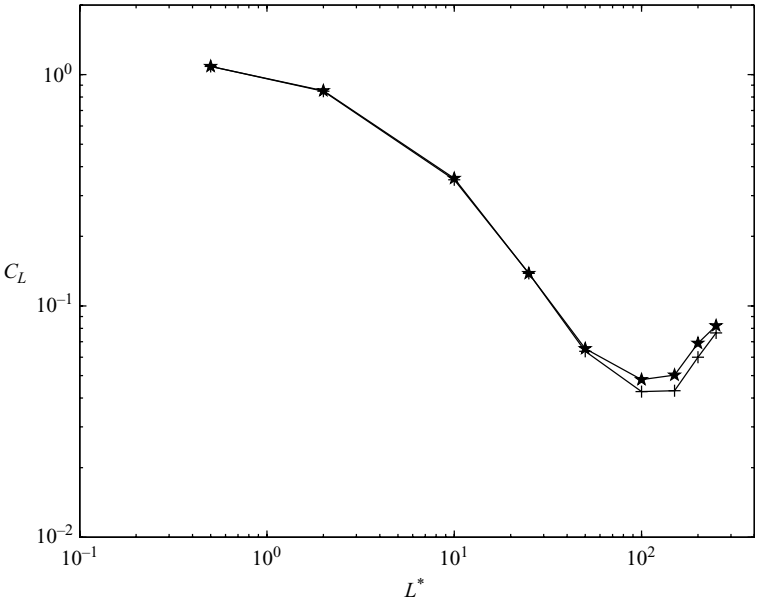

FIGURE 15. Lift coefficients for non-rotating and torque-free rotating spheres at $L = 1$: $-+-$, non-rotating; $-\bigstar-$, torque-free rotating.

The small effect of torque-free rotation on drag and lift forces, and hence on the translational motion of the sphere, over a wide Reynolds number range has been discussed in the context of an unbounded shear flow by Bagchi & Balachandar (2002). The present results for a sphere translating parallel to a plane wall show similar behaviour. The additional contribution from sphere rotation can be expressed in terms of a Magnus lift coefficient as the difference

$$C_{L,Mg}(Re, \Omega_{st}) = C_L(Re, \Omega_{st}) - C_L(Re, \Omega_{st} = 0). \tag{16}$$

Rubinow & Keller (1961) showed the Magnus lift force on a spinning sphere in the Stokes limit to be $C_{L,Mg} = \Omega d/|U|$, where Ω is the angular velocity of the spinning sphere and U is the relative velocity between the sphere and the ambient flow. Figure 16 plots the Magnus lift coefficient obtained from the present simulations, normalized by $\Omega_{st} d/|U|$, against Re for the different separation distances considered. Except for very small Reynolds numbers the present results fall within the range 0.5 to 0.7. This behaviour is consistent with the results of Bagchi & Balachandar (2002), who observed the ratio $C_{L,Mg}/(\Omega_{st} d/|U|)$ to be about 0.55 for the case of a spinning sphere in an unbounded linear shear flow. The experiments of Tanaka, Yamagata & Tsuji (1990) and Tri, Oesterle & Deneu (1990) observed this ratio to be about 0.4 and 0.25, respectively. The quantitative difference between the present results and the others can be attributed to the influence of the wall. Nevertheless, in all these cases the Magnus contribution to lift force appears to linearly scale with $\Omega_{st} d/|U|$.

4.6. *Unsteady regime*

Here we extend the present simulations to Reynolds numbers above 250 into the unsteady regime. For all four separation distances, the results for $Re = 250$, 270, and 300 are listed in table 3. At $Re = 250$ for all four separation distances the flow remains steady. In an unbounded uniform flow it is well established that the wake behind a sphere remains steady at $Re = 250$ (Taneda 1956; Magarvey & Bishop 1961;

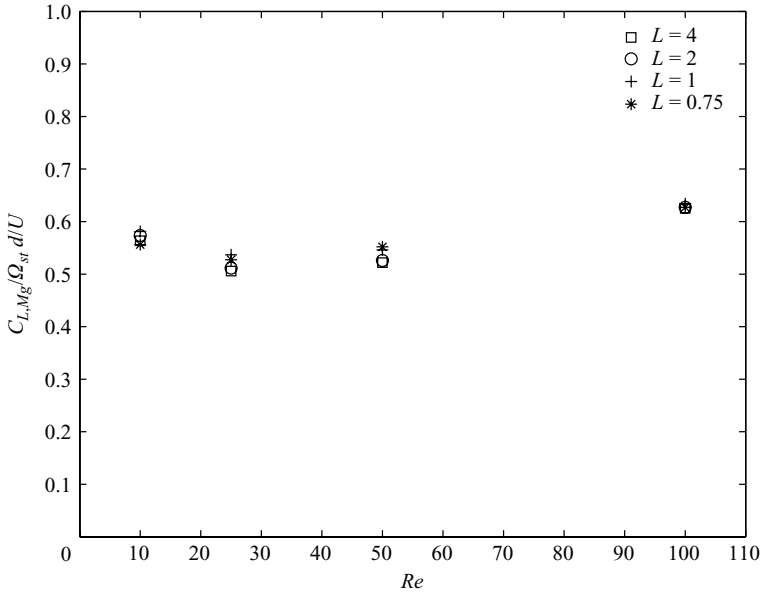

FIGURE 16. The scaled Magnus lift coefficient computed as given in (16). The symbols for the different separation distances from the wall are the same as in figure 7.

L	$Re = 250$	$Re = 270$	$Re = 300$
0.75	$C_L = 1.063 \times 10^{-1}$	$C_L = 1.056 \times 10^{-1}$	$C_L = 1.034 \times 10^{-1}$
1	$C_L = 7.649 \times 10^{-2}$	$C_L = 7.895 \times 10^{-2}$ $C'_L = 8.485 \times 10^{-3}$ $St = 1.531 \times 10^{-1}$	$C_L = 7.935 \times 10^{-2}$ $C'_L = 2.063 \times 10^{-2}$ $St = 1.556 \times 10^{-1}$
2	$C_L = 6.345 \times 10^{-2}$	$C_L = 6.787 \times 10^{-2}$ $C'_L = 3.277 \times 10^{-3}$ $St = 1.323 \times 10^{-1}$	$C_L = 6.978 \times 10^{-2}$ $C'_L = 1.415 \times 10^{-2}$ $St = 1.361 \times 10^{-1}$
4	$C_L = 6.165 \times 10^{-2}$	$C_L = 6.630 \times 10^{-2}$ $C'_L = 1.537 \times 10^{-3}$ $St = 1.337 \times 10^{-1}$	$C_L = 6.858 \times 10^{-2}$ $C'_L = 1.338 \times 10^{-2}$ $St = 1.389 \times 10^{-1}$

TABLE 3. Lift coefficients and Strouhal number for different Re and separation distances.

Natarajan & Acrivos 1993; Tomboulides 1993; Johnson & Patel 1999). For a sphere in a uniform ambient flow, the above experimental and numerical studies suggest a critical Reynolds number of about 270 for the onset of unsteadiness and vortex shedding. In particular, the recent numerical simulations of Johnson & Patel (1999) yield a steady flow at $Re = 270$, and an unsteady flow at $Re = 280$, suggesting a transition somewhere in between.

The presence of a nearby wall influences the onset of unsteadiness in two different ways. The added viscous effect of the wall is to delay the onset of unsteadiness, whereas the asymmetry introduced by the wall can promote early shedding. The results shown in table 3 illustrate the competition between these two opposing mechanisms. For the smallest separation of $L = 0.75$ considered, the flow remains steady even at $Re = 300$; thus, the added viscous effect of the very close wall is to

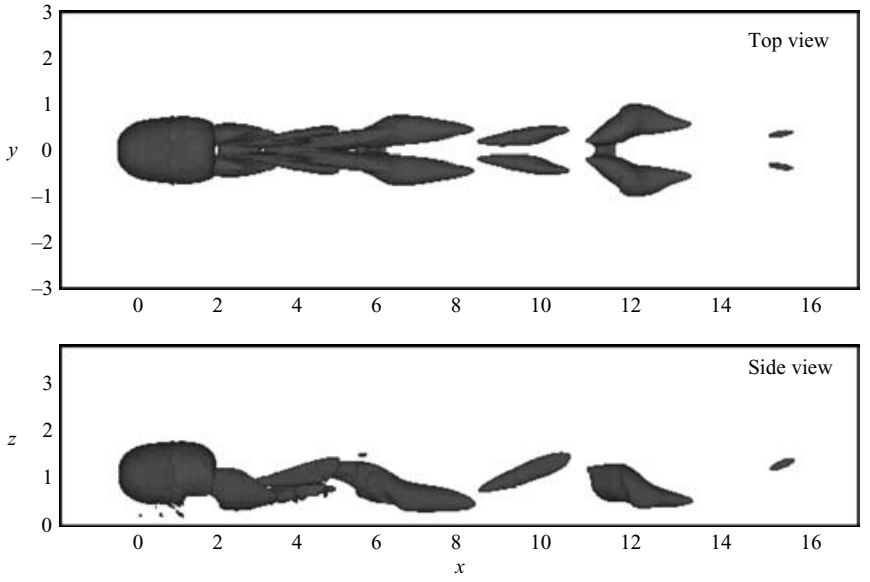

FIGURE 17. Instantaneous vortical structure in the unsteady regime for $Re = 300$ at $L = 1$.

delay the onset of unsteadiness. In contrast, for the other three separation distances the flow is unsteady even at $Re = 270$, and thus a steady-to-unsteady transition occurs somewhere between 250 to 270.

In all the unsteady cases considered, the flow is perfectly periodic, and the non-dimensional shedding frequency is presented in table 3 as the Strouhal number (St). At a fixed distance from the wall, the Strouhal number increases with Re. For the largest separation considered ($L = 4$) at $Re = 300$ the shedding frequency, $St = 0.139$, is in good agreement with the values of 0.136 and 0.137 obtained by Tomboulides (1993) and Johnson & Patel (1999) in the limit of an unbounded uniform flow. The Strouhal number increases by about 15 % as the wall is approached, i.e. for $L = 1$.

For each of the unsteady cases the table also lists the amplitude of lift fluctuation (C_L'). From the amplitude of lift fluctuation it is clear that at $L = 4$ the flow is barely unsteady and the critical Reynolds number is just below 270. With further increase in separation distance, the critical Reynolds number is likely to increase above 270 as $L \to \infty$, consistent with the results of Johnson & Patel (1999). Between $L = 4$ and $L = 1$ the critical Reynolds number decreases well below 270 but remains above 250. As separation distance further decreases to $L = 0.75$, the critical Reynolds number rapidly increases above 300.

The mean lift coefficient for increasing Re from 250 to 300 illustrates the saturation process addressed in § 4.3. For the smallest separation distance, the lift coefficient has already begun to decrease as Re increases above 250. For the intermediate separations ($L = 1$ and 2) the lift coefficient continues to monotonically increase from $Re = 250$ to $Re = 300$. However, the rate of increase slows down, clearly suggesting saturation with further increase in Re above 300.

Figure 17 shows the vortical structure of the wake region in the unsteady regime. Vortex shedding is one sided with interconnected hairpin vortex loops, similar to that observed by Johnson & Patel (1999) for the uniform flow case. Unlike in an unbounded uniform flow, the plane of symmetry of the wake vortical structure is dictated to be

normal to the wall. Thus, the time-dependent transverse force arising from the one-sided vortex shedding is along the wall-normal direction.

5. Conclusions

Here we discuss results from direct numerical simulations of flow around a rigid sphere moving parallel to a flat wall in an otherwise stagnant ambient fluid. We consider a Reynolds number range from 0.5 to 300 at four different separation distances between the wall and the centre of the sphere equal to 0.75, 1, 2, and 4 sphere diameters.

The present results at the lowest Reynolds number are in good agreement with the asymptotic results of Vasseur & Cox (1977). At higher Reynolds numbers, from about 1 to 100, the computed lift coefficients are in good agreement with the model proposed by Takemura & Magnaudet (2003), based on their experimental measurements. Above $Re \approx 100$ we observe an interesting trend of increasing lift coefficient, which eventually saturates above a Reynolds number of about 250, when the flow becomes unsteady. This down-and-up trend in the lift coefficient agrees with the computational results of Kim *et al.* (1993) for two side-by-side spheres settling in stagnant fluid. This trend is also seen in both the pressure and skin friction components. The wake behind the sphere undergoes an imperfect bifurcation, resulting in the development of a double-threaded vortex structure. This bifurcation is akin to that in an unbounded ambient flow at $Re \approx 210$, where the axisymmetry of the wake gives way to a plane of symmetry. The formation of the double-threaded wake appears to be responsible for the increase in lift.

At small separation distances the effect of the wall is to increase the drag coefficient above that of an unbounded uniform flow. At intermediate distances, however, the effect of the wall can result in a small, but finite, reduction in the drag coefficient below that of a uniform flow. Thus, at all finite Re considered, the asymptotic approach to uniform flow result (as $L \to \infty$) is from below. This behaviour is consistent with the low-Re results of Vaseeur & Cox (1977). We observe the drag coefficient for all separations and Re to be well fitted by: $C_D = (24/Re)(1 + (3/8)Re) + 66.654/L^* - 8.364$.

Due to the presence of the wall, the sphere experiences a net hydrodynamic moment about the y-axis. At low Re the moment coefficient is negative, but it rapidly increases and becomes positive even with a small increase in Re. With further increase in Re the moment coefficient reaches a positive peak and slowly decays to very small values. The present moment coefficients at the higher Reynolds numbers are compared with those obtained by Kim *et al.* (1993).

In addition to non-rotating spheres we considered the effect of free rotation, where the sphere is allowed to rotate in response to hydrodynamic torque acting on it and to reach a final torque-free steady state. The direction and magnitude of terminal angular velocity of the rotating sphere are consistent with the moment coefficient measured for the non-rotating spheres. The effect of torque-free sphere rotation on the drag force is negligible. The effect of rotation is to increase the lift coefficient slightly, and the increase can be estimated as a Magnus lift contribution with a scaling factor of about 0.5 to 0.7. This behaviour is similar to that observed for a freely rotating sphere in an unbounded linear shear flow (Bagchi & Balachandar 2002).

In many applications the particle motion near a wall is in the presence of a boundary layer flow. Here, the lift force has wall-induced, shear-induced, and rotation-induced contributions. The present results indicate a simple superposition of the wall-induced and rotation-induced mechanisms. It is not clear if such simple superposition of

the different mechanisms will be valid in the presence of an ambient shear flow. Superposition will certainly simplify the problem, since all three mechanisms are now reasonably well established over a range of Reynolds number. At finite Re, the validity of such superposition can be questioned. Future experiments and computations are needed to further elucidate on this important point.

Simulations were extended to Reynolds numbers above 250 to explore the onset of unsteadiness. The results of Johnson & Patel (1999) show that in an unbounded uniform ambient flow, the wake becomes unsteady between 270 and 280. For the largest separation considered ($L = 4$), we observe the wake to become unsteady at Re slightly below 270. With decreasing separation distance from the wall from $L = 4$ to $L = 1$, the critical Re for onset of unsteadiness further decreases below 270 (but remains above 250). As the separation distance decreases further to $L = 0.75$ the critical Re dramatically increases, perhaps due to the dominant stabilizing viscous effect of the nearby wall. At this separation distance the flow remains steady even at $Re = 300$.

This research was supported by the ASCI Center for the Simulation of Advanced Rockets at the University of Illinois at Urbana-Champaign through the US Department of Energy (subcontract number B341494). The National Center for Supercomputing Applications (UIUC) is also acknowledged, for the use of their computational facilities.

REFERENCES

Bagchi, P. & Balachandar, S. 2002 Effects of free rotation on the motion of a solid sphere in linear shear flow at moderate *Re*. *Phys. Fluids* **14**, 2719–2737.

Bagchi, P., Ha, M. Y. & Balachandar, S. 2001 Direct numerical simulation of flow and heat transfer from a sphere in a uniform cross-flow. *Trans. ASME: J. Fluids Engng* **123**, 347–358.

Cherukat, P. & McLaughlin, J. B. 1990 Wall-induced lift on a sphere. *Intl J. Multiphase Flow* **16**, 899–907.

Cherukat, P. & McLaughlin, J. B. 1994 The inertial lift on a rigid sphere in a linear shear flow field near a flat wall. *J. Fluid Mech.* **263**, 1–18.

Clift, R., Grace, J. R. & Weber, M. E. 1978 *Bubbles, Drops, and Particles*. Academic.

Cox, R. G. & Hsu, S. K. 1977 The lateral migration of solid particles in a laminar flow near a plane. *Intl J. Multiphase Flow* **3**, 201–222.

Faxen, H. 1921 Einwirkung der gerfaβwande auf den Widerstand gegen die bewegung einer kleinen kugel in einer zahen flussigkeit. PhD Dissertation, University of Upsala.

Faxen, H. 1924 Der widerstand gegen die bewegung einer starren kugel in einer zahen flussigkeit die zwischen zwei parallelen ebenen wanden eingeschlossen ist. *Ark. Matematik, Astronomi och Fysik* **18**, 1–52.

Fischer, P. 1997 An overlapping Schwarz method for spectral element solution of the incompressible Navier-Stokes equations. *J. Comput. Phys.* **133**, 84–101.

Johnson, T. A. & Patel, V. C. 1999 Flow past a sphere up to a Reynolds number of 300. *J. Fluid Mech.* **378**, 19–70.

Kim, I., Elghobashi, S. & Sirignano, W. A. 1993 Three-dimensional flow over two spheres placed side by side. *J. Fluid Mech.* **246**, 465–488.

Kok, J. B. 1993 Dynamics of a pair of gas bubbles moving through liquid Part I. Theory. *Eur. J. Mech.* B/*Fluids* **12**, 515–540.

Magarvey, R. H. & Bishop, R. L. 1961 Transition ranges for three-dimensional wakes. *Can. J. Phys.* **39**, 1418–1422.

Magnaudet, J., Takagi, S. & Legendre, D. 2003 Drag, deformation and lateral migration of a buoyant drop moving near a wall. *J. Fluid Mech.* **476**, 115–157.

Natarajan, R. & Acrivos, A. 1993 The instability of the steady flow past spheres and disks. *J. Fluid Mech.* **254**, 323–344.

Rubinow, S. I. & Keller, J. B. 1961 The transverse force on a spinning sphere moving in a viscous fluid. *J. Fluid Mech.* **11**, 447–459.

Saffman, P. G. 1965 The lift on a small sphere in a slow shear flow. *J. Fluid Mech.* **22**, 385–400.

Takemura, F. & Magnaudet, J. 2003 The transverse force on clean and contaminated bubbles rising near a vertical wall at moderate Reynolds number. *J. Fluid Mech.* **495**, 235–253.

Takemura, F., Takagi, S., Magnaudet, J. & Matsumoto, Y. 2002 Drag and lift forces on a bubble rising near a vertical wall in a viscous fluid. *J. Fluid Mech.* **461**, 277–300.

Taneda, S. 1956 Studies on wake vortices (III). Experimental investigation of the wake behind a sphere at low-Reynolds-number. *Rep. Res. Inst. Appl. Mech., Kyushu Univ.* **4**, 99–105.

Tanaka, T., Yamagata, K. & Tsuji, Y. 1990 Experiment on fluid forces on rotating sphere and spheroid. *Pro. 2nd KSME-JSME Fluids Engineering Conference*. vol. 1, p. 366.

Tomboulides, A. G. 1993 Direct and large eddy simulation of wake flows: Flow past a sphere. PhD thesis, Princeton University, Princeton, NJ.

Tri, B. D., Oesterle, B. & Deneu, F. 1990 Premiers resulats sur la portance d'une sphere en rotation aux nombres de Reynolds intermediaies. *C. R. Acad. Sci. Paris* II **311**, 27–31.

Vasseur, P. & Cox, R. G. 1977 The lateral migration of spherical particles sedimenting in a stagnant bounded fluid. *J. Fluid Mech.* **80**, 561–591.

Zhou, J., Adrian, R. J., Balachandar, S. & Kendall, T. M. 1999 Mechanisms for generating coherent packets of hairpin vortices in channel flow. *J. Fluid Mech.* **387**, 353–396.